Journal of
Materials Chemistry A

Materials for energy and sustainability

Accepted Manuscript

This article can be cited before page numbers have been issued, to do this please use: B. Liu, X. Duan, C. Yuan, L. Wang, J. Li, D. P. Finegan, B. Feng and J. Xu, *J. Mater. Chem. A*, 2021, DOI: 10.1039/D0TA12082K.

View Article Online
DOI: 10.1039/D0TA12082K

Quantifying and modeling of stress-driven short-circuit in lithium-ion batteries in electrified vehicles

Binghe Liu [a*], Xudong Duan [b, c*], Chunhao Yuan [d, e], Lubing Wang [f, g], Jiani Li [d, e], Donal P. Finegan [h], Bill Feng [i], Jun Xu [d, e†]

[a]*School of Automotive Engineering, Chongqing University, Chongqing 400044, China*

[b]*Vehicle Energy & Safety Laboratory (VESL), Beihang University, Beijing, China, 100191*

[c]*Department of Automotive Engineering, School of Transportation Science and Engineering, Beihang University, Beijing 100191, China*

[d] *Department of Mechanical Engineering and Engineering Science, The University of North Carolina at Charlotte, Charlotte, NC 28223, USA.*

[e]*Vehicle Energy & Safety Laboratory (VESL), North Carolina Motorsports and Automotive Research Center, The University of North Carolina at Charlotte, Charlotte, NC 28223, USA.*

[f]*Safety Engineering, Ministry of Education, Ningbo University, Ningbo 315211, China*

[g]*Department of Mechanics and Engineering Science, Faculty of Mechanical Engineering & Mechanics, Ningbo University, Ningbo 315211, China*

[h]*National Renewable Energy Laboratory, 15013 Denver West Parkway, Golden CO 80401, USA*

[i]*Jaguar Land Rover, Coventry, CV34LF, UK*

[*]These authors contributed equally.

[†]Corresponding author: Prof. Jun Xu at jun.xu@uncc.edu; Tel: (704)-687-8240; Fax: (704)-687-8240

View Article Online
DOI: 10.1039/D0TA12082K

View Article Online
DOI: 10.1039/D0TA12082K

Abstract

Despite the huge expansion of electric vehicle sales in the market, customers are discouraged by the possible catastrophic consequences brought by the safety issues of lithium-ion batteries, such as internal short circuits, especially in crash scenarios. Herein, we reveal the quantitative relation between the deformations of the battery and the internal short circuit. By designing *in-situ*, *ex-situ* observation and post-mortem characterization of the component materials, we quantify the stress-driven internal short circuit and failure behavior of the component material. With the aid of the validated numerical computational model as well as the *in-situ* characterization of the global-field temperature, we successfully identify the minor and major short circuits of the cells upon various mechanical abusive loadings. Finally, we establish the internal short circuit criteria for typical formats of batteries. This discovery also provides a fundamental understanding of both internal and external stress-driven short circuits in a much broader context.

Keywords: Battery safety; Stress-driven; Internal short-circuit; Modeling; Experimental characterization

View Article Online
DOI: 10.1039/D0TA12082K

Introduction

Powered by lithium-ion batteries (LIBs), electrified vehicles (EVs) are important ways to achieve global energy optimization and environment sustainability [1-4]. Unlike other industrial products, electrified vehicles experience much more complicated scenarios, especially for abusive conditions such as mechanical crashes, overheating, and overcharging [5-7], which may trigger battery safety issues. With the advancement of battery science and technology, high energy-/power-density batteries have recently become available in the latest electrified vehicles with satisfactory power output and driving range [8]. On the other hand, such progress poses even more intractable but catastrophic safety problems with higher-energy-density batteries in larger numbers in electrified vehicles.

Generally, the internal short circuit (ISC) is regarded as the initial and milestone safety event followed by possible thermal runaway, even fire/explosion [9-11]. External factors such as mechanical abusive loading, and internal factors such as active particle expansion/fracture/fragmentation, Li dendrite growth, all lead to failure of the battery component materials and stress-driven ISC. Therefore, safety issues of LIB were first studied at the cell level where controllable mechanical loading, such as compression [12-14], indentation [13-15], bending [12, 16, 17], penetration [18], was applied to the cells directly. Typical load-, temperature-, voltage-time (displacement) curves were recorded and thus provided a direct relation between the mechanical deformation response of the cell and the internal short circuit behavior by monitoring the voltage drop. However, the major drawbacks of the studies are the lack of *in-situ* experimental

View Article Online
DOI: 10.1039/D0TA12082K

characterization during the cell deformation process that hinders our understanding of the mechanism of the short circuit upon mechanical abusive loading. Later, the X-ray computed tomography and radiography were developed with built-in thermal sensors to conduct the *operando* characterization of a cell [19, 20] with the resolution at the magnitude of 10 μm. Due to the temporal and spatial resolution limitation, it is also difficult to capture the separator failure during the deformation before/on the triggering of the ISC. Note that it is technically difficult to conduct *in-situ*/*operando* characterization for such a complicated structure upon large mechanical deformation with a satisfactory resolution.

Numerical modeling and simulation, on the other hand, provides a sharp tool with available in-depth physical and mechanics details for our further understanding. Naturally, the first numerical modeling for the battery upon mechanical abusive loading was established in the homogenized fashion where separator, cathode, and anode are considered as a homogeneous material [12, 21] . The following work by considering more complicated mechanical factors such as dynamic loading and the electrochemistry status were established [22, 23]. More recently, an advanced mechanical model which considers all detailed description of every layer of anode, cathode, and separator [24]. In the meantime, for battery safety problem, it is not sufficient even we have a high-fidelity numerical model to describe the mechanical response of the cell; instead, a reasonable mechanics-based short circuit criterion should be established based on the model. As such, a few phenomenological stress- and strain-based criteria were suggested [12, 25-32] but only valid for major ISC where the voltage drop is unrecoverable and significant [22, 26, 33]. Due to the lack of an

View Article Online
DOI: 10.1039/D0TA12082K

underlying mechanism description for the short circuit, such criteria only possess limited generality.

Herein, to quantify the relationship between short circuit and mechanical deformation in batteries from a fundamental perspective, we leverage a combination of experimental characterization and numerical modeling. Firstly, mechanical behaviors of the battery component materials are characterized by both *in-situ* and *post-mortem* experiments. The numerical models for all component materials are established and validated by the *ex-situ* experiments. ISC modes are then identified and categorized based on the characteristic mechanisms through the in-depth analysis based on the model. The model provides insights into how the ISC issues can be improved by the rational design of electrode material, separator, and the entire structure, and opens a new perspective for a game-changing ISC monitoring and early warning.

Mechanical behavior characterization of the components

Anode, cathode, and separator are dominant components within the battery to experience significant deformations during mechanical loadings of the cell. Here, we combined experiments and finite element method to analyze the mechanical failure behavior of each component (Al foil of 10 um thickness, separator of 11 um thickness, cathode of 110 um thickness, Cu foil of 20 um and anode of 120 um) in various stress states, including in-plane tension, out-of-plane compression, and indentation loadings (See the Method part).

(1) Characterization of the tensile behaviors of the component materials

View Article Online
DOI: 10.1039/D0TA12082K

The cathode and anode consisting of the foil and coating (including active particles and binders) both exhibit typical elastoplastic behaviors in tension (Figs. 1(a) and (b)). However, different failure behaviors were observed through the *in-situ* observation by an optical microscope with a magnification of 1000. For the cathode, the crack first initiated from Point 1 and appeared within the foil area, where the force/stress started to decrease (Fig. 1(a) and Video 1). Then the crack propagated from the foil to the neighboring coating along the in-plane direction. Finally, the cathode fractured at Point 3, and the force dropped to zero. For the anode, the interface of the coating and foil started to debond at Point 1 caused by the strain mismatch at the interface between the foil and coating, which led to the slight drop of the load (Fig. 1(b) and Video 2). Then the debonding interfaces further propagated, and the load kept decreasing. The cracks propagated throughout the coating at Point 3. From Points 3 to 4, the cracks started to initiate and propagated in the foil (Cu) until the whole anode structure fractured. In the meantime, the separator demonstrated slight anisotropicity (the stress-strain curves in four different directions (0°, 90°, ± 45°) are close to each other)). Thus, we adopted the mechanical behavior of separator by averaging those four curves (Fig. 1(c)). The fracture of the separator was triggered at Point 1, and the load dropped immediately and here, we use elastoplastic to model the constitutive behaviors.

Based on the constitutive relations characterized by the experiments, we established the computational model of the three component materials based on the finite element method (See the Method part). The excellent agreement between experimental and computational results demonstrate the success of the modeling (Figs. 1 (a) – (c)).

View Article Online
DOI: 10.1039/D0TA12082K

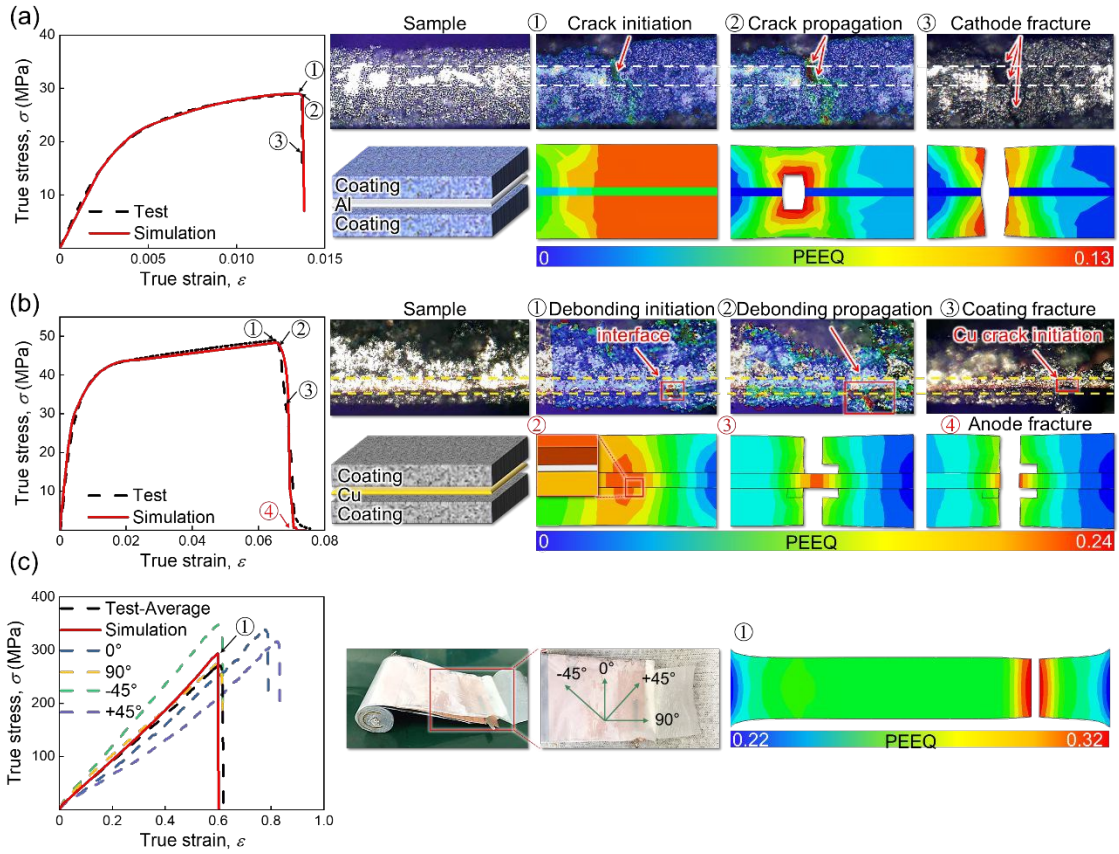

Fig.1 The constitutive true stress-strain curves, structures of samples, failure morphologies from experiments (the color indicates deformation density obtained from the digital image correlation (DIC)) and equivalent plastic strain (PEEQ) field from FEM of (a) cathode, (b) anode, and (c) separator samples during tensile loadings. Due to the anisotropic mechanical properties of the dry-processed separator, mechanical tests were performed at different angles.

(2) Characterization of the compressive behaviors of the component materials

In most scenarios, the component materials are subjected to compressive loadings. Here, we adopt the stacking compression tests in the out-of-plane direction. Note that to maintain the integrity of all the component materials to the greatest extent, we stacked the anode and separator together because the separator and anode were bonded together during the manufacturing process and very difficult to be separated. Crushable foam-like behaviors are observed in both cathode and composite of anode and separator (Figs. 2(a) and (b)). We also established the computation model

View Article Online
DOI: 10.1039/D0TA12082K

to describe the compressive behaviors of the materials, and the model can capture the mechanical behaviors of the materials satisfactorily.

The *in-situ* observation for the inner structure is challenging in such abusive loading conditions. Thus, *ex-situ* characterization was then adopted after unloading at each force level (Table S2). For the cathode, Fig. 2(a) exhibits the morphology of the cathode samples at two force levels. At Point1, there was no sign of mechanical damage in the sample, while fractures were observed in the four sides of the sample at Point 3. The numerical model exhibits the same phenomena at these two force levels. From the validated model, we found that the foil and coating failed simultaneously due to material failure as the equivalent plastic strain (PEEQ) field and the curves show at Stage 2.

For the composite of anode and separator (Fig. 2(b)), to demonstrate the representative result, we use the 3rd layer of the composite close to the indenter (See Method) as a typical result to reveal the failure sequence of the foil and separator. We removed the coatings (active particles and binders), leaving only the foil attached to the separator (Fig. S1), to observe the cracks in the foil more clearly for the *ex-situ* characterizations. Cracks/damage did not start to develop in both the foil layer and separator until Point 3 (both in the experiment and numerical model). The computational model indicates that the damage of the foil is initiated at the corner when the true strain $\varepsilon = 0.526$ while the separator remained intact during Stage 2 and fractured at Point 3. It proves that the foil fractures earlier than the separator under compression when the anode and separator are stacked together.

View Article Online
DOI: 10.1039/D0TA12082K

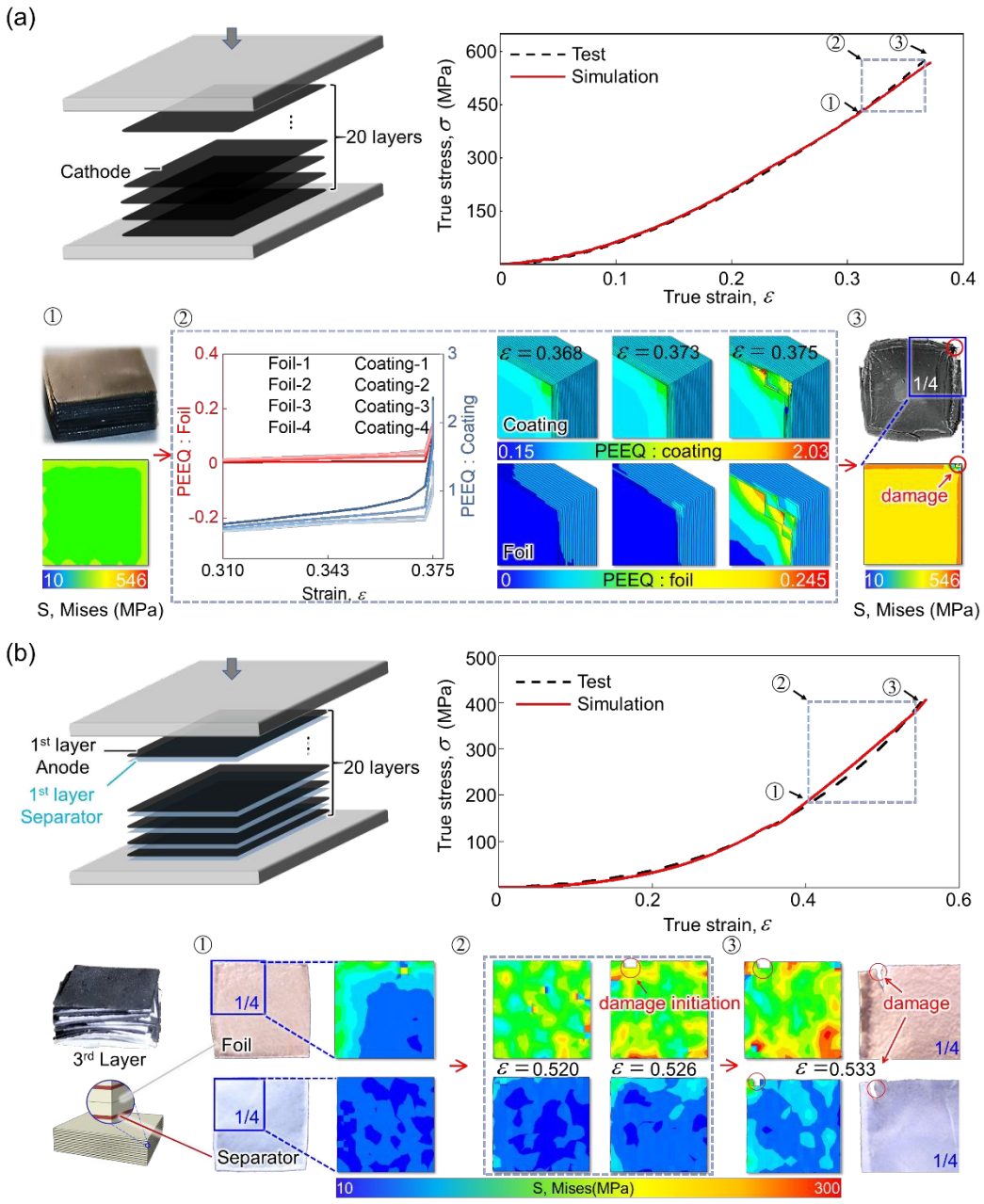

Fig.2 The constitutive true stress-strain curves, equivalent plastic strain (PEEQ)/stress field and failure morphologies of the (a) cathode, (b) composite of anode and separator during out-of-plane compression loadings. ① and ②are the force levels ex-situ characterization adopted, and simulation and experiment results are compared at these two points. ③shows the simulation results from ① to ②.

(3) Characterization of the indentation behaviors of the component materials

To investigate the material behaviors in a more complicated stress status, we designed the indentation tests based on the stacking layers, i.e., stacks of the cathode layers and stacks of the

View Article Online
DOI: 10.1039/D0TA12082K

composite anode-separator layers, and indentation models were also established (See the Method part). Note that the coatings were also removed after unloading to observe the cracks in the foil (Fig. S1).

For the cathode stack (Fig. 3(a)), the cracks of 1st-layer foil started to occur at Point 2. Soon, the cracks propagated, and the indenter penetrated into the cathodes layer by layer. Small cracks of the 4th-layer foil started to occur at Point 3. These phenomena were both found in the experiment and simulation. Referred to the indentation model, we can observe that the 1st-layer coating cracks start to initiate at Point 1, which indicates the earlier failure for coating than the foil under the indentation loading.

For the composite anode-separator stack (Fig. 3(b)), the force was loaded at Points 1 and 3 and unloaded, respectively, for the *ex-situ* characterization. After unloading, each layer of the sample was observed through the microscope with a scale of 500 to show the small cracks. The test results confirmed that no cracks were observed both in 1st-layer foil and separator at Point 1 and when the indentation reached Point 3, the failure/cracks propagated to the 6th layer, while the 7th-layer foil and separator still remained complete. The model can predict these phenomena successfully (Fig. 3(b)). For more detailed information in the numerical simulation, we can find that the failure of the 1st-layer separator happens at Point 1, but no cracks are initiated. After the indentation displacement of about 0.02 mm beyond Point 1, the cracks of the 1st-layer anode (foil) appears at Point 2. The indenter then penetrates into the composite of separator and anode layer by layer. When the indentation reaches Point 3, more failure/cracks are observed in 5th-layer foil

View Article Online
DOI: 10.1039/D0TA12082K

than in 5th-layer separator, which is also supported by the sample morphology in the tests (Fig. 3 (b)).

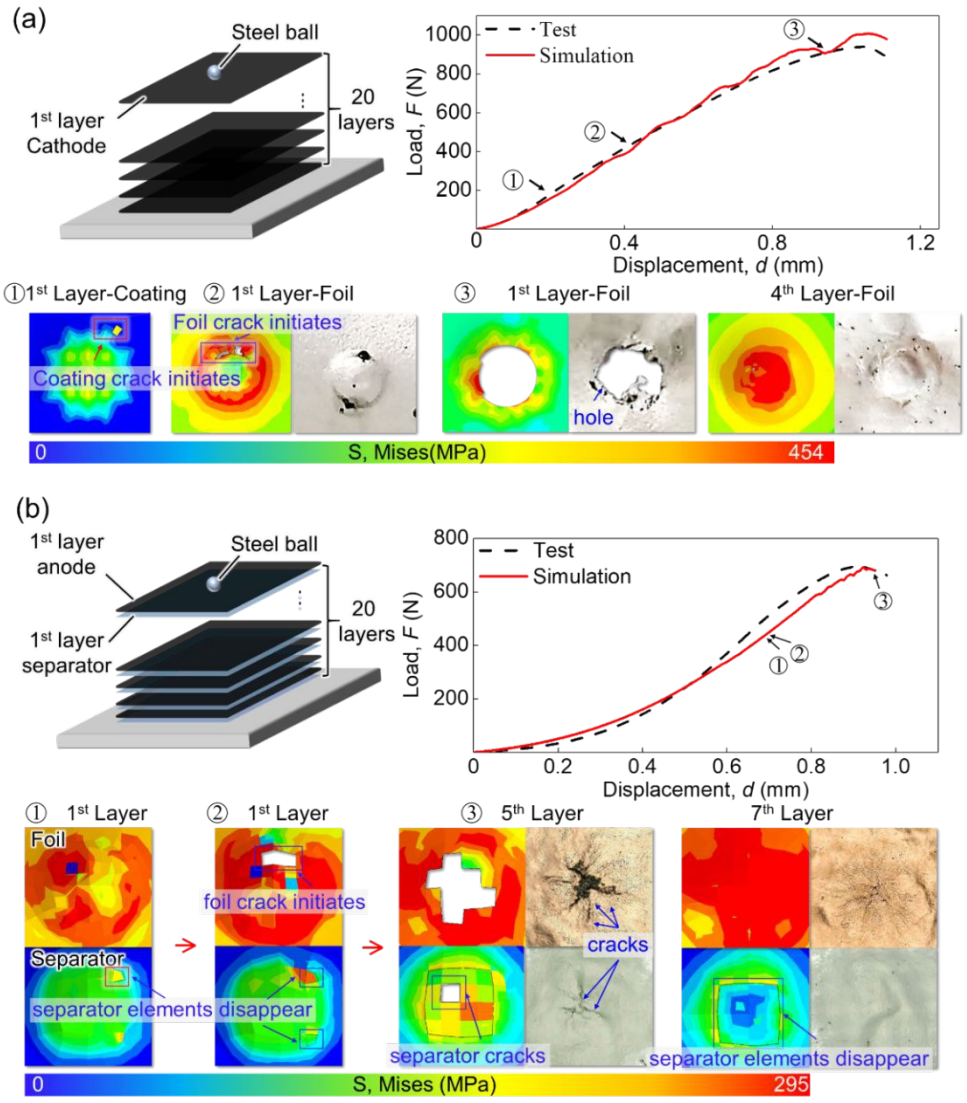

Fig.3 The load-displacement curves, stress field distribution, and failure morphologies of the (a) cathode, (b) composite of anode and separator during indentation loadings.

It needs to be pointed out that the samples used in the mechanical tests were all obtained from the battery sample charged to 0.1 SOC. Our previous studies [34, 35] have explored the SOC effect on mechanical behaviors of components in a battery, including electrodes and the separator. It is discovered that the cathode and separator were independent on the SOC value; however, the anode

View Article Online
DOI: 10.1039/D0TA12082K

showed obvious SOC dependence. A recent research[36] reported that there were two different mechanisms competing with each other in the anode during mechanical tests exposing to air, and it might be unable to explain the stress-strain behavior of the anode under 100% SOC satisfactorily. The SOC dependence of anode is so complicated that it needs more sophisticated tests and analyses and is an ongoing research topic. We can use the method provided in Ref. [34] to establish the relationship between the mechanical parameters and SOC for future research.

Stress-driven failure and ISC behavior

An essential step towards the quantitative understanding of stress and ISC needs to have a thorough investigation based on the cell level. To precisely apply the stress on the battery and its component materials in a repeatable way, herein, we adopt the representative mechanical abusive loading—compression loading to the cell. Detailed loading setups can be referred to the Method.

For a cylindrical cell (21700 NCM /graphite cylindrical LIB, 4000 mAh, 2.7-4.2V) upon flat plate compressive loading, ISC is usually detected to happen at Point 6 (Fig. 4(a)), where voltage drops obviously, and temperature increases sharply [37]. Considering such significant voltage drop behavior, we define such ISC as a "major ISC" with a shear voltage drop of more than the order of magnitude of 0.1 V. However, most of the existing studies ignore the "minor ISCs" (or micro ISCs) under mechanical abusive conditions, which may lead to a rising risk to the thermal runaways and even catastrophic safety hazards [38]. The voltage drop of "minor ISC" is small ($\sim 1\mathrm{mV}$) since the resistance of "minor ISC" can be up to $100\,\Omega$ [39]. Here we use the derivative of the voltage, i.e., dU/dt, to observe the voltage changes clearly (Fig. 4(b)).

View Article Online
DOI: 10.1039/D0TA12082K

From the temperature perspective, we can observe no noticeable variation over the temperature field before Point 1 (Fig. 4 (a)). As demonstrated by the thermal imager, a local increase to the temperature of ~18 ℃ was identified in the innermost layer (the 36th layer) at Point 1 (Fig. 4(c)) where the voltage change (dU/dt)-displacement curve started to drop continuously (Fig. 4(b)). In the meantime, the battery impedance started to increase at the deformation of 4.7 mm (Point 1) (Fig. S2). Cell dU/dt curve drop, local temperature rise, and impedance increase together form strong evidence pointing towards the ISC occurrence at Point 1. Thus, we can safely use the dU/dt vs. displacement curve to capture the trigger of the minor ISC—the starting point when dU/dt drops continuously (the identifying methodology is explained in Supplementary Materials, Fig. S3). With further compression, the minor ISC regions extended from the central part of the jellyroll to the outer area before major the ISC occurred, evidenced by the thermal field measurements at Points 2 and 3 which were selected randomly between Points 1 and 4 (Fig. 4(c)).

At Point 4, the temperature started to increase more significantly (over 10 ^{o}C within 1 s), and at Point 5, it started to appear temperature concentration between the 17th to 18th layers where the temperature exceeds more than 5℃ over other areas in the battery bottom section captured by the infrared thermal imager (Fig. 4(c)). Within seconds, the temperature increased to over 100 ^{o}C, and smoke was detected. Point 6 was regarded as the moment of major ISC identified by a shear voltage drop of more than the order of magnitude of 0.1 V. For post-mortem examination, we unloaded the cell at Point 6 and removed the battery case to unfold the jellyroll. We found that the fracture area was located in the area where the maximum temperature resided (within the vicinity between

View Article Online
DOI: 10.1039/D0TA12082K

12th to-18th layers (Fig. 4 (e)). Note that the highest temperature during the compression did not reach the melting point of the foils, suggesting that the cracks in foils were triggered by mechanical loading. Due to the limitation of the detection methodology, we can only determine the location in the radial plane, and the computational model should be established to show the exact location of the ISC also in the axial direction.

An equivalent model (capable for predicting the cell response with fast computational efficiency) and a detailed model (with detailed description of every component materials in the cell with high-fidelity computational accuracy) are established (see Method). As the detailed model illustrated, in the beginning, the deformation of the battery leads to the separation within the inner layers, which makes the voltage change slightly (almost non-detectable from the voltage-displacement curve in Fig. 4(a)). When the displacement reaches Point 1 where the minor ISC was identified in the experiment, the maximum value of PEEQ = 0.2119 appears in the 36th layer of the jellyroll in the equivalent model (Fig. 4(d)). Furthermore, a high-fidelity detailed model with a detailed description of the anode, cathode, and separator is established to represent the equivalent model in the specific layer, i.e., the 36th layer. The computation results show that the separator between the anode and cathode fractures at Point 1 (Fig. 4(d)), leading to the direct contact between the active particles from both anode and cathode. Note that the coatings fracture 0.2 mm in displacement earlier before Point 1, indicating that it is the fracture of separator leading to minor ISCs rather than the coating fracture. Besides, the major ISC is not triggered after the separator fractures because the copper and aluminum foils can still be separated by the failed coatings to

View Article Online
DOI: 10.1039/D0TA12082K

avoid possible contact when foils remain complete under compression loadings. The separator failure area is so limited (Fig. 4(d)) that the ISC resistance during minor ISC is relatively large, i.e., ranging from $100-300\,\Omega\cdot\mathrm{mm}^2$ [37]. That is why minor ISCs cannot be detected merely from the voltage drops.

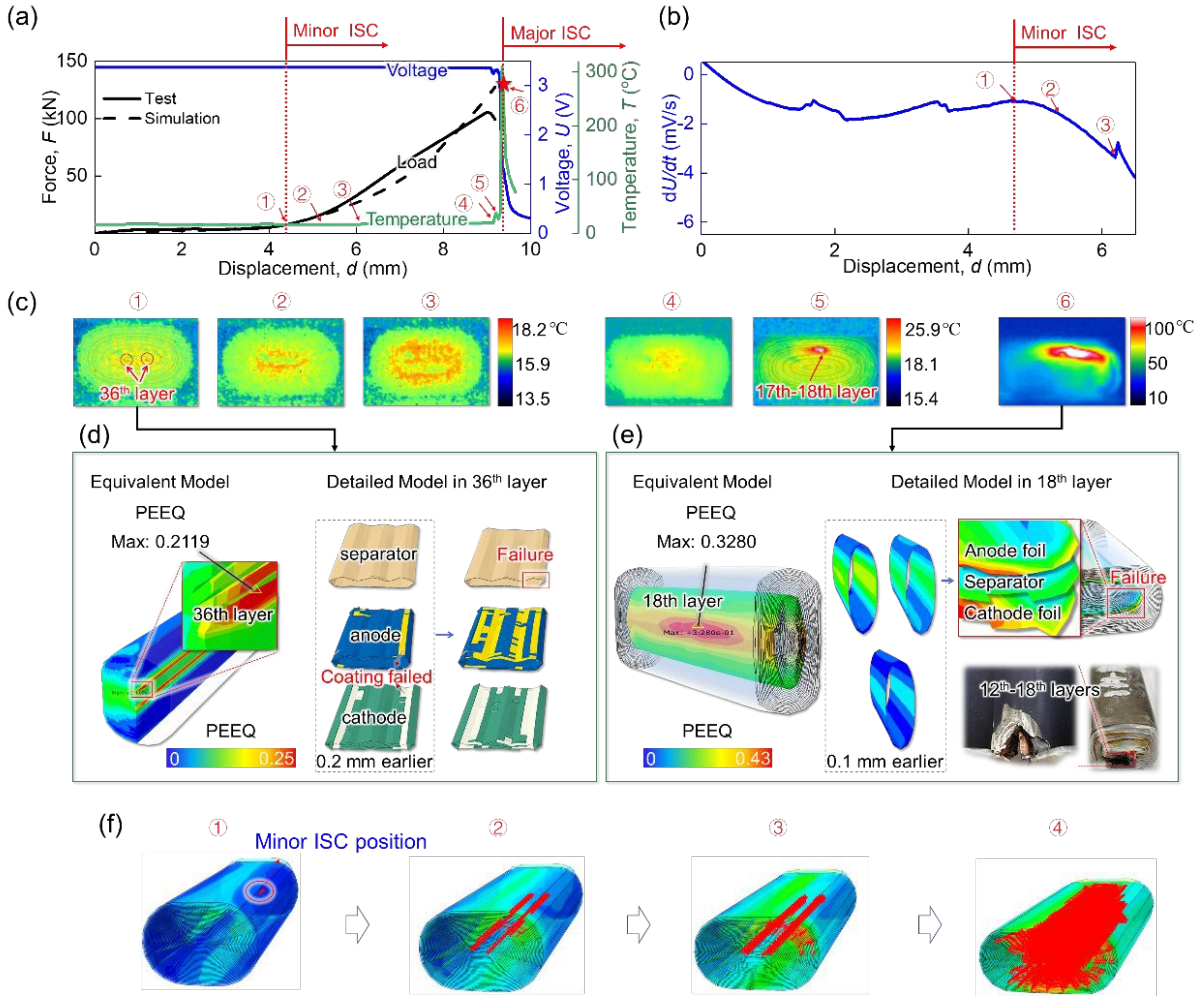

Fig. 4 (a) the voltage-, temperature-, and load-displacement curves, (b) the derivative of the voltage (dU/dt)-displacement curve, (c) temperature field (by thermal imaging), (d) FEM results of LIB under compression loadings at Point 1, (e) FEM results of LIB under compression loadings at Point 6, and (f) The minor ISC position changes under compression (computed by the equivalent model)

Referring to the equivalent model, the minor ISC region (where PEEQ is greater than 0.2119) expands not only in the radial plane but also in the axial direction with the compression loading

View Article Online
DOI: 10.1039/D0TA12082K

(Fig. 4(f)). This will lead to the increase of the ISC resistances, which is considered as the reason for the temperature field expansion (Fig. 4(c)) and the drop of dU/dt (Fig. 4(b)) from Points 1 to 4. At Point 6 where major ISC was triggered in the experiment, we can observe clearly in the equivalent model that the 18th layer of the jellyroll exhibits the maximum value of PEEQ = 0.328. Similarly, with the aid from the high-fidelity model, we can see at Point 6, the separator, foil, and coating failed simultaneously, while they do not fail 0.1 mm earlier (Fig. 4(e)), evidencing that the material failure occurs at Point 6. In this case, due to the cracks of the foil to expose its partial inner material, the active particles and binders can no longer shield the direct contact between the copper and aluminum foils such that the major ISC is triggered.

To reveal the mechanism of the temperature response during the whole compressive process (Fig. 4(a)), we estimate the temperature rises at key points. At Point 1, the separator failed while the foils remained complete, leading to a circuit with an approximate minor ISC resistance $R_{minor} \geq 200\Omega$, and the temperature rise at Point 1 is estimated $\Delta T_1 \leq 2.12℃$ (see Supporting Materials), which makes the temperature curve rise not obvious (Fig. 4a). The related parameters are listed in Table S1.

At Point 6, the simultaneous failure of the separators and electrodes lead to a circuit with a major ISC resistance $R_{major} = 1.5\Omega$ according to the $\Delta U = 0.1V$ determined by the definition of major ISC. The temperature rise at Point 6 can be calculated $\Delta T_2 = 20.36℃$ (see Supporting Materials), which is close to the difference of maximum temperatures obtained from two consecutive images (the time interval is 0.033s) near Point 6 in the thermal imaging video.

View Article Online
DOI: 10.1039/D0TA12082K

Criteria and evolution for stress-driven ISCs

As mentioned in the previous section, both major and minor ISCs were triggered in the compression tests identified by the internal temperature field and the dU/dt curve. Note that the internal temperature field variation is the direct evidence for ISCs. However, it cannot be easily detected when the battery case remains complete. The surface temperature points are used as alternative signals fit for more mechanical abusive conditions and serve as supporting evidence of ISCs. Thus, we developed the identification-method for stress-driven ISCs based on the voltage value and dU/dt curves. The major ISC is identified by obvious voltage drop (~0.1V), while the minor ISC is identified by the starting point of the continuous drop of dU/dt (Fig. S3). Further, we used the methods to identify minor/major ISCs based on the experiment results of three other loading conditions (cylindrical indentation, three-point bending, and offset compression) on the same target batteries (Figs. 5(a)-(c)).

Based on the more efficient-effective equivalent model, and the ISC criteria can be established. The range of the PEEQ is 0.2119-0.2358 for minor ISC, while the range is 0.3280-0.3285 for major ISCs under the four loading conditions (Fig. 4(d) and Fig. 5). It can be safely used as the criteria for the small range differences for these loadings. Thus, the $\overline{\varepsilon}_{\mathrm{eq,minor}}$ and $\overline{\varepsilon}_{\mathrm{eq,major}}$ are set as the critical values of minor and major ISCs separately. And the value of them is given as the conservative lower limits of each range mentioned above ($\overline{\varepsilon}_{\mathrm{eq,minor}} = 0.2119$, $\overline{\varepsilon}_{\mathrm{eq,major}} = 0.3280$), which may avoid missing any possible safety issues as Fig. 6(a) shows. In the future application, the battery can be set as the 'suspicious battery' by this

View Article Online
DOI: 10.1039/D0TA12082K

criterion, and the subsequent state of suspicious batteries can be judged by combining with other means to improve the accuracy of predictions. Note that SOC will affect the critical values of minor and major ISCs (shown in Fig. S4) due to the change of mechanical properties of each component, which means $\bar{\varepsilon}_{\mathrm{eq,minor}}$ and $\bar{\varepsilon}_{\mathrm{eq,major}}$ are SOC-dependent parameters. SOC effect needs to be explored in future studies.

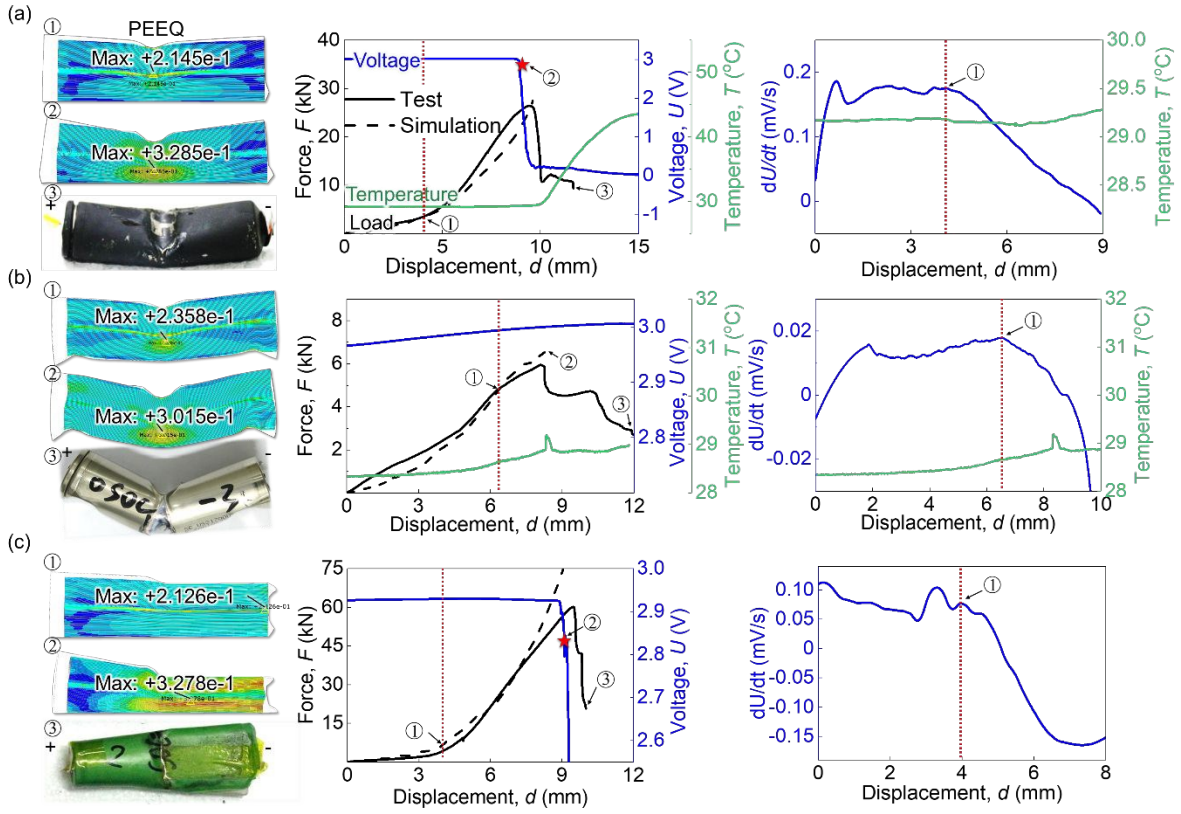

Fig. 5 The PEEQ field from FEM, the morphology of samples, the voltage-, load-, surface temperature-, dU/dt-displacement curves and the markers of minor/major ISCs from experiments (the red dotted line represents the minor ISC and the red star point represents major ISC) under (a) indentation, (b) bending and (c) offset compression loadings

Then the criteria based on the effective equivalent model were used to predict the ISCs in representative mechanical loadings, and the results show great agreement with the repeated experiments (Fig. 6(a)). We discover that the offset compression causes the minor ISC more easily

View Article Online
DOI: 10.1039/D0TA12082K

(at nominal strain *d/R* where *d* is displacement and *R* is the radius of the battery of 0.178) because the local PEEQ at the center of the jellyroll increases fast at the beginning in this loading condition, while the indentation loading triggers the major ISC more easily due to the PEEQ concentration near the indenter. In bending, no major ISC can be triggered. It is also interesting to observe that d*U*/d*t* has the largest varying window (related to the minor ISC degree) in compression loading while it is the smallest in bending condition (Fig. 6 (b)).

To investigate the underlying mechanism, we define the effective minor ISC failure area $S^*_{\text{minor}}=S_{\text{minor}}/S_{\text{jellyroll}}$ where S_{minor} is the area with $\varepsilon_{eq} \geq \bar{\varepsilon}_{\text{eq,minor}}$ and $S_{\text{jellyroll}}$ is the total area of the unfolded jellyroll. For compression and indentation loadings, the minor ISC failure area increases obviously, while almost does not change in the bending loading (Figs. 6 (b)). S^*_{minor} can be regarded as an important factor in predicting the degree of minor ISC. Note that S^*_{minor} should not necessarily be equal to the real-world ISC contact area for estimating ISC resistance, but they have positive correlations. Thus, $\left|\Delta(\mathrm{d}U/\mathrm{d}t)\right|$ (reflecting minor ISC degree experimentally, and related to real-world ISC contact area) and S^*_{minor} have similar trend, shown in Fig. 6(b). Note that $\left|\Delta(\mathrm{d}U/\mathrm{d}t)\right|$ means the absolute value of the difference between current $\mathrm{d}U/\mathrm{d}t$ data and the value of $\mathrm{d}U/\mathrm{d}t$ at minor ISC triggering point equal to $\left|\mathrm{d}U/\mathrm{d}t\text{-}\mathrm{d}U/\mathrm{d}t(t=t_{\text{minor ISC}})\right|$. Then S^*_{minor} can be regarded as the parameters to determine the minor ISC degrees.

Our previous study [40] has established the relationship between the ISC area and ISC resistance (to indicate the ISC degree) written as $R_{ISC}=R_{ISC}^{initial}(1\text{-}S^*_{ISC})$ in the multiphysics model where mechanical, thermal, and electrochemical models were coupled. This relationship was then used

View Article Online
DOI: 10.1039/D0TA12082K

to describe both minor and major ISCs in this study and was modified into $R_{\text{minor}} = R_{\text{minor}}^{initial}(1\text{-}S_{\text{minor}}^{*})$ and $R_{\text{major}} = R_{\text{major}}^{initial}(1\text{-}S_{\text{major}}^{*})$ applied in the multiphysics model developed in Ref. [40] under compression loading (the basic information of the multiphysics model is shown in Supporting Materials). According to the voltage and dU/dt curves (Figs. 6(c) and (d)), the simulation results show good agreement with the experiment both in the evolution of minor and major ISCs. Note that the mechanical model conducted in COMSOL was established in 2D structure, and the critical strain values of minor and major ISCs were modified into 0.2755 and 0.351, respectively.

With the help of embedded sensors[41] such as multipoint film temperature and strain sensors which allows the real-time monitoring of internal temperature/strain field of single cell, the methodologies and models can be further developed and applied in the battery safety real-time monitoring and early warning with various formats and material systems of lithium-ion batteries through the cloud-based battery condition monitoring platform [42] which allows individual battery cells communicate with cloud and the battery model predicts the battery states executed in the cloud, contributing to the next-generation of safer electric vehicles.

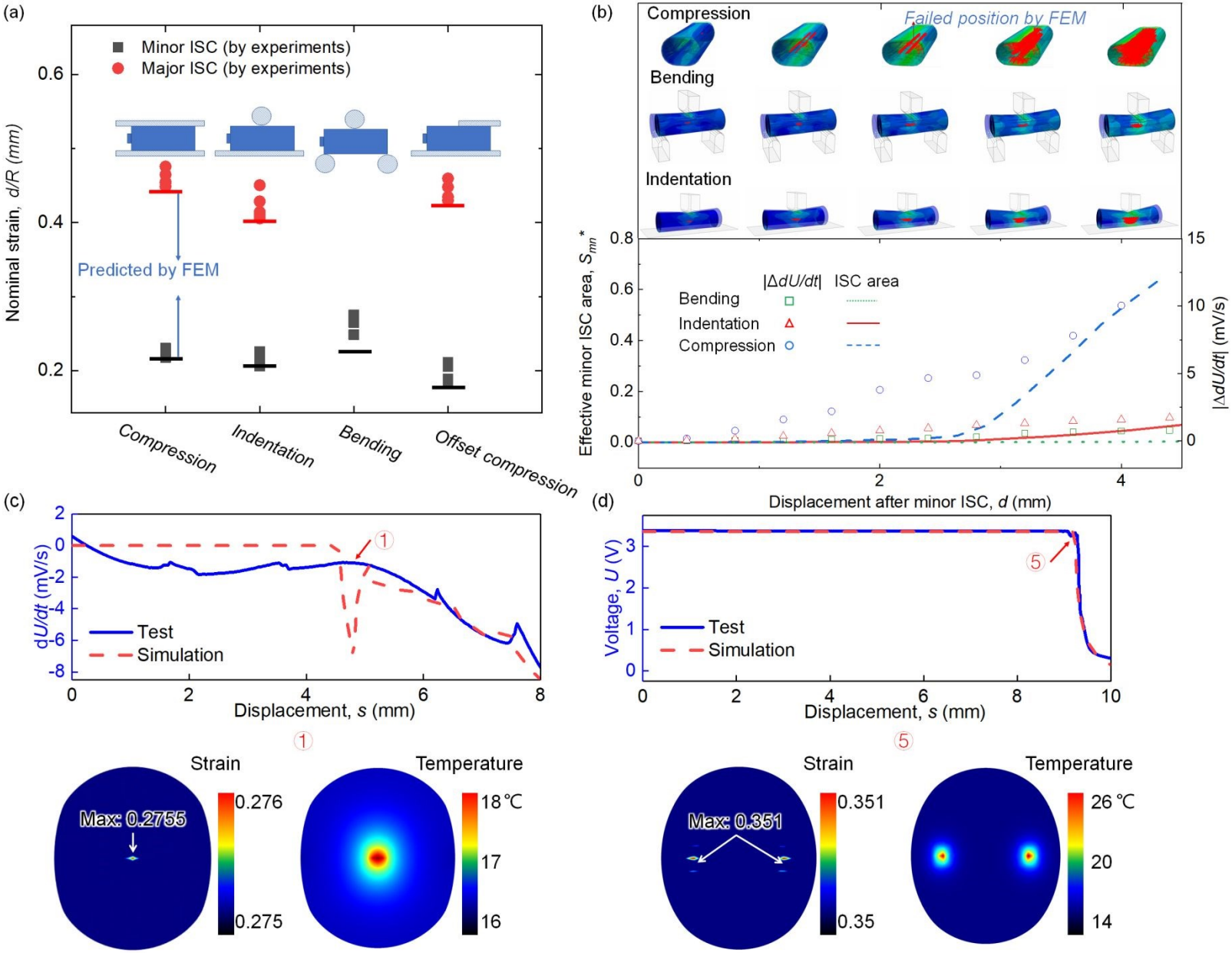

Fig. 6 (a) The prediction result for the ISC criterion in various loading conditions (the line presents the displacement predicted by FEM and the points present the displacements identified from tests), (b) the effective minor ISC failure area, positions and $\left|\Delta(\mathrm{d}U/\mathrm{d}t)\right|$ changes after minor ISCs, (c) dU/dt curves of the test and simulation and the strain and temperature field at Point 1 from Multiphysics model, and (d) voltage curves of the test and simulation and the strain and temperature field at Point 5 from Multiphysics model

View Article Online
DOI: 10.1039/D0TA12082K

Conclusion

In summary, combined with the *in-situ*, *ex-situ,* and post-mortem experimental characterizations, the numerical computational models established and validated here provides a unique mechanistic explanation and quantifying for the stress-driven ISC behavior. The sequence, timing, and behaviors of the mechanical failure of the battery component materials are discovered to be the responsible reasons for the exhibition of ISC phenomena electrochemically. We also established universal minor and major ISC safety criteria and demonstrated the versatility in predicting ISC behaviors in various mechanical abusive loading conditions. Results clear the understanding of the ISC behaviors in the cell and provide some inspirations to protect the batteries from internal short circuit caused by mechanical damage. The minor ISC can be mitigated by increasing the elongation of the separator and reducing the damage area when the separator fractures. To mitigate the major ISC and thermal runaway, there are some efforts on designing structure of the current collector in LIBs such as embrittling the current collector an appropriate microstructure[43], which can help to isolate ISC and heat generating areas.

Method

Specimen preparation

21700 NCM (Nickel Cobalt Manganese Oxide)/graphite cylindrical LIB served as a representative target with a capacity of 4000 mAh with cut-off voltages in charge and discharge are 4.2V and 2.7V, respectively. For safety and convenience to capture the ISC behavior during

View Article Online
DOI: 10.1039/D0TA12082K

experiments, all cells were fully discharged and then charged to 0.1 SOC at 0.1C in advance and all the tests were conducted at the room temperature. The effects of SOC (Fig. S4) and environment temperature on test results are supplemented in the Supporting Material.

This cell is composed of a battery case, a jellyroll (including the cathode, anode, separator, and electrolyte), and a safety valve. The jellyroll starting at 1.24mm from the center of the battery, is winded into 36 circles with a separator-cathode-separator-anode sequence (Fig. S5 (a)). The specific geometric parameters of these components, including thicknesses of each layer, are summarized in Table S3. The electrodes (consisting of the coating and foil) and separator were obtained after assembling the battery sample. The foils of electrodes were separated from the coating to explore the mechanical[34, 35] response and failure morphology of foils, the separation process is concluded in Fig. S1.

Modeling method

(1) Numerical modeling of the component materials

For both anode and cathode, the two-solid-one-shell model (Fig. S5(b)) is adopted consisting of two-layer coating and one-layer foil allowed to be assigned different material properties in each layer. Under tensile loading, both the coating and foil can be regarded as elastic-plastic material [27]. The bond strength at the interface of the cathode is much higher than that of the anode [44], so the coating in the cathode was built based on sharing the same nodes with the foil, while the interface in the anode was modeled by the virtual crack closure technique (VCCT) to characterize debonding behaviors[28]. Representative volume element (RVE) models with $0.1mm \times 1mm \times 0.11mm$ for

View Article Online
DOI: 10.1039/D0TA12082K

cathode and $0.1\text{mm}\times1\text{mm}\times0.12\text{mm}$ for anode were extracted to study their mechanical response. The whole electrode (cathode /anode), including both the foil and coating, was described by solid elements in a total of 2,250 elements. For the separator, it was also modeled as the elastoplastic material based on tensile tests and meshed by 2,400 solid elements according to the actual geometries. All the damage behaviors were defined by the ductile damage model and the failure parameters were calibrated based on the failure behavior and force-displacement curve. The critical mechanical and mesh parameters of the components are summarized in Table S4.

In compression, the coating is the primary component to sustain external force loads, and the mechanical contribution of the foil can be ignored at least before the compaction stage. Thus, the stress-strain curve of the whole electrode (cathode/anode) was regarded as that of the coating [37]. The crushable foam model was applied for coatings to characterize compaction behavior. To make the model still be able to describe the tensile response of the whole electrodes, we transformed the tensile stress-strain curve of the electrodes into foils according to the area fraction of the foil. An elastic-plastic model was still used here. The failure parameters of the foils and coatings were recalibrated based on the force-displacement curve during compression loading and failure behaviors of samples (especially the foils with the coating removed) after unloading. Quarter models were established based on the stacking mode of the electrode samples to take the mechanical symmetric boundary conditions to improve the computational efficiency. The foils were meshed by shell elements, and the interface in the anode was simplified into node merging due to the increasingly close bonding between the foil and coating under compression. Surface-to-

View Article Online
DOI: 10.1039/D0TA12082K

surface contact was used between each layer, and the friction coefficient was set as an empirical value of 0.3. The compression model of the 20-layer cathode was meshed into 54,000 elements in total, and the 20-layer composite of anode and separator contained 18,000 elements in total. The critical settings of the components are summarized in Table S5, and the recalibrated material parameters were then used in the following models, including the indentation model of electrodes and the battery models applied in four loading conditions.

In the indentation model, a 2 mm diameter steel ball placed in the center of the top sample layer was built into a rigid to squeeze the stacks with the friction coefficient of 0.3, and the full models were applied with an increasing mesh density from 0.7mm to 1.25mm within a circular area 2 mm from the center to better capture the contact behaviors. After the mesh convergence study, the indentation models of the cathode and the combination of anode and separator were meshed into 286,946 elements and 68,513 elements, respectively.

In addition, the battery case is meshed using shell elements with an elastoplastic model.

(2) Numerical modeling of the cell

The jellyroll meshed by solid elements is simplified as 36 concentric ring layers [45], and each layer (composing of 1 layer of the anode, 1 layer of the cathode, and 2 layers of the separator) is regarded as one homogenized material with equivalent material properties. The anisotropic properties of the jellyroll were considered in a cylindrical coordinate system, and the specific mechanical properties and mesh information were summarized in Table S5. Four typical loading

View Article Online
DOI: 10.1039/D0TA12082K

conditions, i.e., radial compression, indentation, three-point bending, and offset compression, were established. A surface-to-surface contact method was also used with the friction coefficient of 0.3.

A detailed model was established based on the equivalent model with detailed local description (Fig. S5(b)). In this model, most of the layers use the equivalent model, and the detailed model containing the models of refined electrodes and separator was used to replace the concerned layer of the jellyroll.

These models were all built based on ABAQUS software platform.

Experiment method

(1) Mechanical testing of the component materials

The quasi-static tension experiment of the electrodes, foils, and the separator were conducted by a material testing machine (Instron 2345) with a range of 5kN and accuracy of 0.1N. All the samples for tension were cut into $5\times60mm^2$ with a clamping area of 15mm in length at both ends. An *in-situ* platform consisting of electric support and optical microscope (VHX-6000) (Fig. S6(a)) was set up to record the stretching process of electrodes at 50 frames per second, and the electrode images were extracted every 10 frames from the video. The side section of electrodes was targeted as the photographed surface with a magnification of 1000 to monitor the failure sequence of components in electrodes (Fig. S6(a)). The images were then processed through planar Digital Image Correlation (DIC) implemented in the software GOM Correlate to calculate the principal strain. Since the main purpose of the DIC results is to highlight regions with serious deformation, the color bars were omitted. 0.1mm/min tension speed was set to the electrodes for better in-situ

View Article Online
DOI: 10.1039/D0TA12082K

observation, and the loading speed of foils kept consistent with that of electrodes, while 10 mm/min speed was set to the separator as the quasi-static condition.

Quasi-static compression tests of cathode were carried out by a SUNS UTM5205X electric mechanics testing machine with a load range of 200kN and accuracy of 4N, and of the anode was conducted by Instron 8801 with a load sensor of 100kN and accuracy of 2N. The quasi-static indentation tests of both the cathode and anode were conducted by Instron 2345. All samples were cut into $15\times15mm^2$. Considering the small thickness of the cathodes, we stacked and tested 20 layers of cathodes, and 20-layer composite anode and separator with 10 layers piled up by each other. In indentation tests, a steel ball with a 1mm radius was adopted as the indenter and placed in the center of the top-layer sample (Fig. S6(b)). To eliminate the gap between layers, we applied a preload of 100N on the samples under compression and of 10N under indentation. The loading speed of the compression and indentation is 1 mm/min. A series of compression and indentation tests were conducted with interruptions where the indenter would stop and be retracted back once the force reached the preset value. The tests were repeated twice at each testing scenario to ensure the repeatability (Fig. S7). Foils were obtained from electrodes with the coating removed to allow examination of failure morphology. Note that the top two layers of the composite of the anode and separator cannot be completely obtained after unloading due to bonding with the indenter, so the third layer was the start to be examined. Since the coating cannot remain intact after separating from samples, its failure parameters were determined based on the test curves and the foil response. The specific force levels and the examination method of samples are listed in Table S2. Note that

View Article Online
DOI: 10.1039/D0TA12082K

it was unnecessary to remove the coating in the cathode compression tests since the fracture of the foil was obvious and can be observed directly (Fig. 2(a)).

(2) Mechanical testing of the cell

Four typical loading conditions, including radial compression, indentation, three-point bending, and offset compression, were carried out to study the relationship between mechanical failure and ISC (Fig. S6(c)). The SUNS UTM5205X electric mechanics testing machine was applied as the loading platform equipped with an explosion-proof box, and all the loading speed was set as 6mm/min. In compression experiment, the negative cap of a battery sample was removed before loading and Fluke Ti400x Thermal Camera with a range from -20 ℃ to 650 ℃ and accuracy of $\pm 2°C$ or 2% temperature value presented, was used to detect the temperature distribution of the bottom section. The positive end and exposed anode tab (only the negative cover was removed, retaining the anode tab) were connected to an Agilent 34972A Data Collector to measure LIB terminal voltage with a frequency of 10Hz. During compression tests, the load, displacement, voltage, and temperature distribution were measured fully synchronized. The Electrochemical Workstation (CHI 660) with a data acquisition rate of 500 kHz was additionally applied to test the impedance of the battery sample under different compression displacements and the frequency for original EIS data was measured from 0.02Hz to 10000Hz. When the displacement reached a certain value, stopped loading and tested the sample 3-5 times until the electrochemical impedance spectroscopy results of two consecutive times were very close, and then continued the compression. In the bending and indentation tests, a 10 mm diameter indenter

View Article Online
DOI: 10.1039/D0TA12082K

was used, and the span of two supports of bending tests was set as 50 mm. The battery case remained complete, and the Agilent 34972A was used simultaneously to measure the voltage and temperatures. Two temperature measuring points were chosen to set up on the battery surface right below the indenter. As for offset compression, the compression plate only squeezed half of the sample close to the negative end.

Acknowledgments and funding sources

No founding sources.

View Article Online
DOI: 10.1039/D0TA12082K

Reference

1. C. Y. Wang, G. S. Zhang, S. H. Ge, T. Xu, Y. Ji, X. G. Yang and Y. J. Leng, *Nature*, 2016, **529**, 515-+.

2. J. Lu, Y. J. Lee, X. Y. Luo, K. C. Lau, M. Asadi, H. H. Wang, S. Brombosz, J. G. Wen, D. Y. Zhai, Z. H. Chen, D. J. Miller, Y. S. Jeong, J. B. Park, Z. Z. Fang, B. Kumar, A. Salehi-Khojin, Y. K. Sun, L. A. Curtiss and K. Amine, *Nature*, 2016, **529**, 377-+.

3. K. Bourzac, *Nature*, 2015, **526**, S105-S105.

4. L. W. Ji, Z. Lin, M. Alcoutlabi and X. W. Zhang, *Energ. Environ. Sci.*, 2011, **4**, 2682-2699.

5. J. Wen, Y. Yu and C. Chen, *Mater. Express*, 2012, **2**, 197-212.

6. J. Deng, C. Bae, A. Denlinger and T. Miller, *Joule*, 2020, **4**, 511-515.

7. B. Liu, Y. Jia, C. Yuan, L. Wang, X. Gao, S. Yin and J. Xu, *Energ. Storage Matter.*, 2020, **24**, 85-112.

8. R. Schmuch, R. Wagner, G. Hörpel, T. Placke and M. Winter, *Nature Energy*, 2018, **3**, 267-278.

9. D. P. Finegan, E. Darcy, M. Keyser, B. Tjaden, T. M. M. Heenan, R. Jervis, J. J. Bailey, R. Malik, N. T. Vo, O. V. Magdysyuk, R. Atwood, M. Drakopoulos, M. DiMichiel, A. Rack, G. Hinds, D. J. L. Brett and P. R. Shearing, *Energy & Environmental Science*, 2017, **10**, 1377-1388.

10. J. Deng, C. Bae, J. Marcicki, A. Masias and T. Miller, *Nature Energy*, 2018, **3**, 261-266.

11. Y. Jia, B. Liu, Z. Hong, S. Yin, D. P. Finegan and J. Xu, *J. Mater. Chem. A*, 2020, **8**, 12472-12484.

12. L. Greve and C. Fehrenbach, *J. Power Sources*, 2012, **214**, 377-385.

13. W. J. Lai, M. Y. Ali and J. Pan, *J. Power Sources*, 2014, **248**, 789-808.

14. W. J. Lai, M. Y. Ali and J. Pan, *J. Power Sources*, 2014, **245**, 609-623.

15. G. Yu, Y. Zheng, B. Feng, B. Liu, K. Meng, X. Yang, H. Chen and J. Xu, *Comput. Struct.*, 2017, **193**, 139-154.

16. J. Xu, B. Liu and D. Hu, *Sci Rep-UK*, 2016, **6**, 21829.

17. E. Sahraei, R. Hill and T. Wierzbicki, *J. Power Sources*, 2012, **201**, 307-321.

18. B. Liu, S. Yin and J. Xu, *Applied Energy*, 2016, **183**, 278-289.

19. T. Yokoshima, D. Mukoyama, F. Maeda, T. Osaka, K. Takazawa, S. Egusa, S. Naoi, S. Ishikura and K. Yamamoto, *Journal of Power Sources*, 2018, **393**, 67-74.

20. D. P. Finegan, B. Tjaden, T. M. M. Heenan, R. Jervis, M. Di Michiel, A. Rack, G. Hinds, D. J. L. Brett and P. R. Shearing, *Journal of the Electrochemical Society*, 2017, **164**, A3285-A3291.

21. T. Wierzbicki and E. Sahraei, *J. Power Sources*, 2013, **241**, 467-476.

22. J. Xu, B. Liu, X. Wang and D. Hu, *Applied Energy*, 2016, **172**, 180-189.

23. B. H. Liu, J. J. Zhang, C. Zhang and J. Xu, *Eng. Fail. Anal.*, 2018, **91**, 315-326.

24. L. B. Wang, S. Yin and J. Xu, *J. Power Sources*, 2019, **413**, 284-292.

25. E. Sahraei, J. Campbell and T. Wierzbicki, *J. Power Sources*, 2012, **220**, 360-372.

26. J. Xu, B. Liu, L. Wang and S. Shang, *Eng. Fail. Anal.*, 2015, **53**, 97-110.

View Article Online
DOI: 10.1039/D0TA12082K

27. C. Zhang, J. Xu, L. Cao, Z. Wu and S. Santhanagopalan, *Journal of Power Sources*, 2017, **357**, 126-137.

28. L. Wang, X. Duan, B. Liu, Q. M. Li, S. Yin and J. Xu, *Journal of Power Sources*, 2020, **448**.

29. C. Yuan, L. Wang, S. Yin and J. Xu, *J. Power Sources*, 2020, **467**.

30. W.-J. Lai, M. Y. Ali and J. Pan, *Journal of Power Sources*, 2014, **248**, 789-808.

31. E. Sahraei, E. Bosco, B. Dixon and B. Lai, *Journal of Power Sources*, 2016, **319**, 56-65.

32. Z. X. Pan, W. Li and Y. Xia, *Journal of Energy Storage*, 2020, **27**.

33. W. Li, J. Zhu, Y. Xia, M. B. Gorji and T. Wierzbicki, *Joule*, 2019, **3**, 2703-2715.

34. J. Xu, B. Liu and D. Hu, *Sci Rep*, 2016, **6**, 21829.

35. L. Wang, S. Yin, C. Zhang, Y. Huan and J. Xu, *Journal of Power Sources*, 2018, **392**, 265-273.

36. Z. Pan, T. Sedlatschek and Y. Xia, *Journal of The Electrochemical Society*, 2020, **167**.

37. B. Liu, Y. Jia, J. Li, S. Yin, C. Yuan, Z. Hu, L. Wang, Y. Li and J. Xu, *Journal of Materials Chemistry A*, 2018, **6**, 21475-21484.

38. W. Gao, Y. Zheng, M. Ouyang, J. Li, X. Lai and X. Hu, *IEEE Transactions on Industrial Electronics*, 2019, **66**, 2132-2142.

39. D. H. Doughty, *Vehicle battery safety roadmap guidance*, National Renewable Energy Lab.(NREL), Golden, CO (United States), 2012.

40. B. Liu, H. Zhao, H. Yu, J. Li and J. Xu, *Electrochim. Acta*, 2017, **256**, 172-184.

41. P. Wang, X. Zhang, L. Yang, X. Zhang, M. Yang, H. Chen and D. Fang, *Extreme Mechanics Letters*, 2016, **9**, 459-466.

42. A. Adhikaree, T. Kim, J. Vagdoda, A. Ochoa and Y. Lee, Cincinnati, OH, USA, 2017.

43. M. Wang, A. V. Le, D. J. Noelle, Y. Shi, Y. S. Meng and Y. Qiao, *Journal of Power Sources*, 2017, **349**, 84-93.

44. J. Zhu, X. Zhang, H. Luo and E. Sahraei, *Applied Energy*, 2018, **224**, 251-266.

45. L. Wang, S. Yin and J. Xu, *J. Power Sources*, 2019, **413**, 284-292.

View Article Online
DOI: 10.1039/D0TA12082K

Figure legends

Fig.1 The constitutive true stress-strain curves, structures of samples, failure morphologies from experiments (the color indicates deformation density obtained from the digital image correlation (DIC)) and equivalent plastic strain (PEEQ) field from FEM of (a) cathode, (b) anode, and (c) separator samples during tensile loadings. Due to the anisotropic mechanical properties of the dry-processed separator, mechanical tests were performed at different angles.

Fig.2 The constitutive true stress-strain curves, equivalent plastic strain (PEEQ)/stress field and failure morphologies of the (a) cathode, (b) composite of anode and separator during out-of-plane compression loadings. ① and ②are the force levels ex-situ characterization adopted, and simulation and experiment results are compared at these two points. ③shows the simulation results from ① to ②.

Fig.3 The load-displacement curves, stress field distribution, and failure morphologies of the (a) cathode, (b) composite of anode and separator during indentation loadings.

Fig. 4 (a) the voltage-, temperature-, and load-displacement curves, (b) the derivative of the voltage (dU/dt)-displacement curve, (c) temperature field (by thermal imaging), (d) FEM results of LIB under compression loadings at Point 1, (e) FEM results of LIB under compression loadings at Point 6, and (f) The minor ISC position changes under compression (computed by the equivalent model)

Fig. 5 The PEEQ field from FEM, the morphology of samples, the voltage-, load-, surface temperature-, dU/dt-displacement curves and the markers of minor/major ISCs from experiments (the red dotted line represents the minor ISC and the red star point represents major ISC) under (a) indentation, (b) bending and (c) offset compression loadings

Fig. 6 (a) The prediction result for the ISC criterion in various loading conditions (the line presents the displacement predicted by FEM and the points present the displacements identified from tests), (b) the effective minor ISC failure area, positions and $\left|\Delta(\mathrm{d}U/\mathrm{d}t)\right|$ changes after minor ISCs , (c) dU/dt curves of the test and simulation and the PEEQ and temperature field at Point 1 from Multiphysics model, and (d) voltage curves of the test and simulation and the PEEQ and temperature field at Point 5 from Multiphysics model.